Title

Bayesian optimization of periodic multilayered slabs for passive absorptivity control

Authors

Kazuma Isobe[*1], Tsuyoshi Yamamoto[1], Yutaka Yamada[1], and Akihiko Horibe[1]

[1] Department of Advanced Mechanics, Graduate School of Environmental, Life, Natural Science and Technology, Okayama University, Tsushima-naka 3-1-1, Kita-ku, Okayama 700-8530, Japan

[*]**Corresponding Author**

Kazuma Isobe

E-mail: isobe.k.ad@okayama-u.ac.jp

Keywords

Radiative cooling, sunlight absorption, Bayesian optimization, vanadium dioxide, short-range surface plasmon polariton.

Abstract

A vanadium dioxide (VO_2) film grown on a titanium oxide crystal shows a metal–insulator transition at room temperature with drastically changed optical properties. A multilayered slab with a sub-micron scale VO_2 film was proposed to utilize its unique properties for passive intensity control of sunlight absorption and radiative cooling. Its optimal geometries were numerically explored using the Bayesian optimization (BO) method. BO was applied for three types of multilayered slabs, those having one, two, or three isolated slabs of different widths. For each type of multilayered slab, BO could optimize geometric variables with practical calculation times considering the total number of possible combinations of variables, which is subsequently referred to as the total number of candidates. Optimization results revealed that two isolated slabs had the most suitable spectral absorptivity in both hot and cold environments. The infrared absorptivity of the double slab was kept low in cold conditions to suppress radiative cooling. However, the double slab exhibited good radiative cooling performance under hot conditions. Electromagnetic energy density surrounding the slab illustrated that metallic VO_2 and gold placed in a parallel manner excited the coupled mode of surface plasmon polaritons to enhance absorptivity. Radiative cooling faded for the triple slab because each slab could couple with radiation propagating only across a portion of the cross-sectional area. Through three BO trials, improvement of the VO_2 visible reflectivity was recognized as a future issue for further development of passive sunlight absorption control.

1. Introduction

The atmosphere contains several gas species that absorb thermal radiation from the Earth's surface. Since representative gases, such as H_2O, CO_2, and O_3, absorb broadband infrared radiation, the atmosphere has a limited transparency band between the wavelengths of 8–13 μm, called the atmospheric window. Radiative coolers with high emissivity in the atmospheric window band were proposed to promote thermal emissions from the Earth's surface into outer space [1,2]. Several radiative coolers also have high reflectivity at visible wavelengths to promote sunlight reflection [3]. Therefore, they are useful for reducing air-conditioning loads in summer. Conversely, their reflection and radiative properties possibly increase heating loads in winter with weak sunlight and low absolute humidity. Researchers also examined thermochromic materials to create a body that switches its reflection and radiative properties depending on its temperature [4]. Examples of thermochromic materials are vanadium dioxide (VO_2) and perovskite-type manganese oxide, which transition to different crystal structures and change their thermophysical properties at certain temperatures [5]. Since their transition temperatures are affected by their chemical structure, numerous studies have tried to control the transition point so that it occurs at a lower temperature. For example, tungsten-doped VO_2 exhibits a phase transition at around 20~30 °C, while pure VO_2 generally shows a phase transition at 68 °C [5–7]. Moreover, a VO_2 film deposited by reactive sputtering has a low phase transition temperature due to strain in the crystal, even if it is pure VO_2 [8,9]. The transition temperature of a VO_2 film grown on a rutile titanium dioxide (TiO_2) substrate oriented to a (001) plane is also reduced to 27 °C because the lattice constant of

rutile TiO_2 is quite close to that of metallic VO_2 (m-VO_2) [10]. Reduced transition temperature is also observed for the TiO_2–VO_2 superlattice [11].

Nanometer-sized structures containing VO_2 have been proposed to control spectral radiative properties at infrared wavelengths [12]. By placing square-shaped VO_2 pieces on an insulator film deposited on a metal substrate, the emissivity of the multilayered film is dependent on its temperature. This is because the transition of VO_2 shifted the wavelength of the plasmonic resonance for the multilayer. VO_2 also attracts researchers' attention to control near-field radiative transfer originating from surface plasmons excited on the VO_2 surface [13,14]. The phase transition feature of VO_2 can be utilized as a thermal diode to rectify the radiative flux exceeding the blackbody limit due to the near-field radiative transfer. For far-field use, a multilayer utilizing optical interference in addition to plasmonic resonance was also proposed to simultaneously control the emissivity at visible and mid-infrared wavelengths [15]. These multilayers still had difficulties with the bandwidth of radiative cooling under hot conditions. Since the Earth's surface emits radiation throughout the day and night, broadband emissions in the infrared range should be promoted through development of a reasonable design. A candidate material for this is multilayered with various widths of multiple strips that correlate to plasmonic resonance at several frequencies [16]. A way to reduce the transition temperature should also be developed to further improve these multilayers. Doped tungsten slightly suppresses the transmittance of insulating VO_2 (i-VO_2) and it causes degradation of switching characteristics [7]. Similar suppression of transmittance was observed for VO_2 deposited by reactive sputtering [17]. Therefore, inserting a TiO_2

layer as a buffer between VO_2 and other materials is the most promising approach. In this study, a suitable multilayer dimension with multiple widths of VO_2 slabs on a TiO_2 layer was investigated using Bayesian optimization to resolve the remaining issues. Moreover, the relation between geometric parameters and plasmonic resonance, which enhances radiative cooling, was analyzed to obtain insights for further improvement.

2. Numerical simulation

Figure 1 shows a schematic diagram of a periodic slab made of TiO_2 and VO_2 placed on a gold substrate. The TiO_2 and VO_2 layers have thicknesses of t_1 and t_2 nm, respectively. Each slab has a width of w_1, w_2, or w_3 nm and they are periodically placed with a pitch of Λ nm. A normal spectral absorptivity of the periodic slab for a transverse magnetic (TM) wave was numerically calculated using a two-dimensional finite difference time domain (FDTD) method. In the current study, slabs with different widths were periodically placed only in the x-direction, forming a one-dimensional array of slabs. It is known that the absorptivity for a transverse electric (TE) wave becomes the same as that for a TM wave in the case of a two-dimensional array of square-shaped slabs [18]. Moreover, when the slab widths are identical, the absorptivity of a one-dimensional slab for the TM wave approximately corresponds to that of a square-shaped slab. Therefore, simulations were conducted in two-dimensional computational domains, and evaluation of absorptivity for a TE wave was omitted in this study to conserve computational resources. The simulation code was developed in Python employing an open-source library [19]. In the FDTD simulation, electric permittivities of gold, VO_2, and TiO_2 were expressed by summation of Drude or Lorentz oscillator models. The relative permittivity of gold [20] was fitted according to the Drude model:

$$\varepsilon_{\mathrm{Gold}}(\omega) = \varepsilon'_{\mathrm{Gold}} + i\varepsilon''_{\mathrm{Gold}} = \varepsilon_\infty - \frac{\omega_\mathrm{p}^2}{\omega(\omega + i\Gamma_\mathrm{p})}. \quad (1)$$

Here, ε_∞ is the background permittivity, ω_p is the plasma frequency, and Γ_p is the carrier relaxation rate. The permittivity of m-VO_2 [21] was fitted to the Drude–Lorentz mixed

model:

$$\varepsilon_{\mathrm{m-VO_2}}(\omega) = \varepsilon'_{\mathrm{m-VO_2}} + i\varepsilon''_{\mathrm{m-VO_2}} = \varepsilon_\infty - \frac{\omega_\mathrm{p}^2}{\omega(\omega + i\Gamma_\mathrm{p})} + \sum_{j=1}^{4} \frac{f_{\mathrm{l}j}\omega_{\mathrm{l}j}^2}{\omega_{\mathrm{l}j}^2 - \omega^2 - i\Gamma_{\mathrm{l}j}\omega}. \quad (2)$$

In this equation, f_{lj} (j = 1, 2, ..., 7) is the Lorentzian oscillator strength, ω_{lj} is the central frequency of the oscillator, and Γ_{lj} is the damping factor. The permittivity of i-VO_2 [21] was fitted to a heptapole Lorentz model:

$$\varepsilon_{\mathrm{i-VO_2}}(\omega) = \varepsilon'_{\mathrm{i-VO_2}} + i\varepsilon''_{\mathrm{i-VO_2}} = \varepsilon_\infty + \sum_{j=1}^{7} \frac{f_{\mathrm{l}j}\omega_{\mathrm{l}j}^2}{\omega_{\mathrm{l}j}^2 - \omega^2 - i\Gamma_{\mathrm{l}j}\omega}. \quad (3)$$

In this study, both states of VO_2 were treated as isotropic media. TiO_2 was modelled as an anisotropic material with the following permittivity tensor [20]:

$$\varepsilon_{\mathrm{TiO_2}}(\omega) = \begin{pmatrix} \varepsilon_{\mathrm{TiO_2\_\perp}}(\omega) & 0 & 0 \\ 0 & \varepsilon_{\mathrm{TiO_2\_\perp}}(\omega) & 0 \\ 0 & 0 & \varepsilon_{\mathrm{TiO_2\_\parallel}}(\omega) \end{pmatrix}. \quad (4)$$

Here, $\varepsilon_{\mathrm{TiO_2\_\perp}}$ and $\varepsilon_{\mathrm{TiO_2\_||}}$ are permittivities of TiO_2 perpendicular and parallel to the c-axis. In the current configuration, the c-axis of the TiO_2 layer is parallel to the z-axis in absolute coordinates. The VO_2 layer contacts the (001) plane of the TiO_2 crystal, aiming to reduce the transition temperature. The extraordinary component, $\varepsilon_{\mathrm{TiO_2\_||}}$, was fitted to a tripole Lorentz model:

$$\varepsilon_{\mathrm{TiO_2\_\parallel}}(\omega) = \varepsilon'_{\mathrm{TiO_2\_\parallel}} + i\varepsilon''_{\mathrm{TiO_2\_\parallel}} = \varepsilon_\infty + \sum_{j=1}^{3} \frac{f_{\mathrm{l}j}\omega_{\mathrm{l}j}^2}{\omega_{\mathrm{l}j}^2 - \omega^2 - i\Gamma_{\mathrm{l}j}\omega}. \quad (5)$$

The ordinary component, $\varepsilon_{\mathrm{TiO_2\_\perp}}$, was fitted to a pentapole Lorentz model:

$$\varepsilon_{\mathrm{TiO_2\_\perp}}(\omega) = \varepsilon'_{\mathrm{TiO_2\_\perp}} + i\varepsilon''_{\mathrm{TiO_2\_\perp}} = \varepsilon_\infty + \sum_{j=1}^{5} \frac{f_{\mathrm{l}j}\omega_{\mathrm{l}j}^2}{\omega_{\mathrm{l}j}^2 - \omega^2 - i\Gamma_{\mathrm{l}j}\omega}. \quad (6)$$

Dielectric parameters used in this study are listed in Table 1. Unlike the complicated dispersion in permittivity, the relative magnetic permeabilities of all materials in this study were set to 1.0 because these materials generally do not show a magnetic response at near infrared frequencies. The boundaries of the computational area in the *x*-direction are a periodic boundary condition, while both boundaries in the *z*-direction are a perfectly matched layer (PML).

Simulations in this study were conducted using two personal workstations with respective 12-core (Ryzen 9 3900X; AMD, Santa Clara, California, United States) and 32-core (Ryzen Threadripper 3970X; AMD, Santa Clara, California, United States) processors.

Table 1 Fitting parameters of dielectric functions

Parameter	Gold	m-VO_2	i-VO_2	TiO_2(∥)	TiO_2(⊥)
ε_∞ (—)	3.97	3.33	1.83	1.40	2.41
ω_p (rad/s)	1.21×10^{16}	4.70×10^{15}	—	—	—
Γ_p (rad/s)	1.23×10^{14}	1.61×10^{15}	—	—	—
f_{l1} (—)	—	1.28	2.92	1.69	4.00
ω_{l1} (rad/s)	—	4.51×10^{15}	5.81×10^{15}	9.93×10^{15}	6.99×10^{15}
Γ_{l1} (rad/s)	—	1.78×10^{15}	5.80×10^{15}	2.55×10^{15}	2.70×10^{15}
f_{l2} (—)	—	49.9	2.00	4.23	0.78
ω_{l2} (rad/s)	—	3.10×10^{14}	3.40×10^{15}	6.47×10^{15}	1.09×10^{14}
Γ_{l2} (rad/s)	—	3.05×10^{14}	3.64×10^{15}	1.20×10^{15}	1.75×10^{13}
f_{l3} (—)	—	1.96	1.51	123	2.50
ω_{l3} (rad/s)	—	2.27×10^{14}	1.58×10^{15}	3.52×10^{13}	9.60×10^{13}
Γ_{l3} (rad/s)	—	2.80×10^{13}	8.30×10^{14}	1.20×10^{13}	4.20×10^{12}
f_{l4} (—)	—	45.4	2.32	—	0.93
ω_{l4} (rad/s)	—	1.15×10^{14}	1.18×10^{14}	—	7.24×10^{13}
Γ_{l4} (rad/s)	—	8.47×10^{13}	2.14×10^{13}	—	3.08×10^{12}
f_{l5} (—)	—	—	0.70	—	63.9
ω_{l5} (rad/s)	—	—	9.60×10^{13}	—	3.65×10^{13}
Γ_{l5} (rad/s)	—	—	9.40×10^{12}	—	3.10×10^{12}
f_{l6} (—)	—	—	0.59	—	—
ω_{l6} (rad/s)	—	—	7.71×10^{13}	—	—
Γ_{l6} (rad/s)	—	—	4.89×10^{12}	—	—
f_{l7} (—)	—	—	7.30	—	—
ω_{l7} (rad/s)	—	—	5.99×10^{13}	—	—
Γ_{l7} (rad/s)	—	—	1.07×10^{13}	—	—

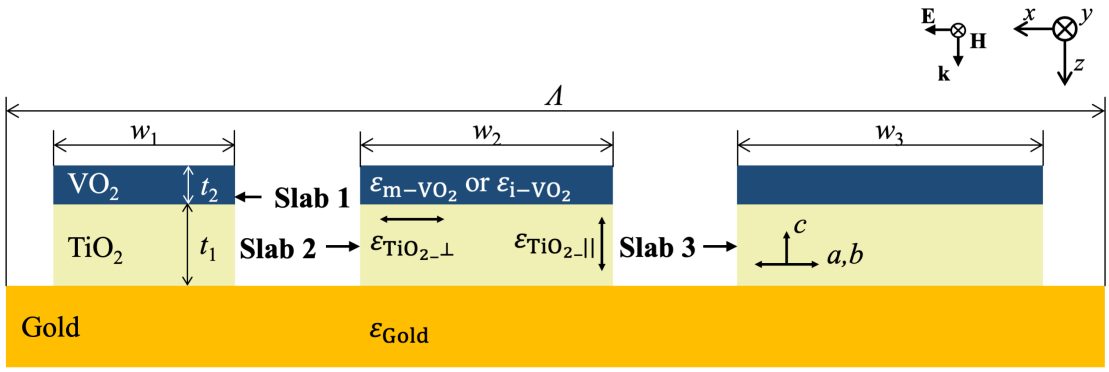

Fig. 1 Schematic diagram of the multilayered slabs periodically placed on a gold base layer.

3. Bayesian optimization

Geometric parameters for the periodic slab were determined and optimized using a Bayesian optimization (BO) method to modify broadband spectral emissivity [22–24]. First, the figures of merit (FOMs) for the radiative heat flux at both high and low temperatures were defined for a quantitative performance evaluation as follows:

$$\mathrm{FOM_{hot}} = \int_{\lambda = 2.5\ \mu\mathrm{m}}^{\lambda = 20\ \mu\mathrm{m}} \left(1 - \alpha_{\mathrm{atm}}(\lambda)\right)\varepsilon(\lambda)E_{\mathrm{bb}}(\lambda, T_{\mathrm{hot}})\mathrm{d}\lambda - \frac{t_{\mathrm{daylight,s}}}{t_{\mathrm{day}}}\int_{\lambda = 0.3\ \mu\mathrm{m}}^{\lambda = 2.5\ \mu\mathrm{m}} \varepsilon(\lambda)E_{\mathrm{AM1.5}}(\lambda)\mathrm{d}\lambda, \quad (7)$$

$$\mathrm{FOM_{cold}} = \frac{t_{\mathrm{daylight,w}}}{t_{\mathrm{day}}}\int_{\lambda = 0.3\ \mu\mathrm{m}}^{\lambda = 2.5\ \mu\mathrm{m}} \varepsilon(\lambda)E_{\mathrm{AM1.5}}(\lambda)\mathrm{d}\lambda - \int_{\lambda = 2.5\ \mu\mathrm{m}}^{\lambda = 20\ \mu\mathrm{m}} \left(1 - \alpha_{\mathrm{atm}}(\lambda)\right)\varepsilon(\lambda)E_{\mathrm{bb}}(\lambda, T_{\mathrm{cold}})\mathrm{d}\lambda, \quad (8)$$

where, α_{atm} is the zenith absorptivity spectrum at the ground, ε represents the spectral emissivity of the slab, E_{bb} is the spectral emissive power of a blackbody at temperature T, $E_{\mathrm{AM1.5}}$ depicts the power of solar radiation (air mass 1.5) [25], $t_{\mathrm{daylight,s}}$ (= 14.5 h) and $t_{\mathrm{daylight,w}}$ (= 10.0 h) are the daylight time in summer and winter months at mid-latitude regions, and t_{day} (= 24 h) is the number of hours in one day. The temperatures at the hot and cold conditions, T_{hot} and T_{cold}, are respectively 303 and 278 K. These are examples of average temperatures in summer and winter, and daily variations of temperature were assumed to cancel out. The zenith absorptivity spectrum was calculated using the HITRAN database according to the reference forward model (RFM) [26,27]. The absorptivity considered the absorption of H_2O, CO_2, O_3, N_2O, CO, CH_4, O_2, NO, NO_2, HNO_3, OH, ClO, N_2, HCN, and HO_2. In summer, the heat flux of radiative cooling

improves the FOM, while sunlight absorption degrades it. Conversely, in winter, the heat flux of radiative cooling suppresses the FOM, while sunlight absorption increases it. When the FOM_{hot} or FOM_{cold} of a product takes a positive value, the product can reduce or increase the surrounding temperature without an active air-conditioner. However, when each FOM takes a negative value, an air-conditioner needs to expend energy at levels proportional to the absolute value of the FOMs to maintain the ambient temperature. In practical situations, FOMs should be much larger than zero to apply the product as a perfect passive air-conditioner because convective heat transfer increases thermal loads for both temperature cases. The total FOM for one geometry is defined as the sum of the FOMs under both temperatures:

$$\mathrm{FOM_{total}} = \mathrm{FOM_{hot}} + \mathrm{FOM_{cold}}. \quad (9)$$

When the FOM_{total} value is positive, the product can save more energy than it consumes using an air-conditioner at any temperature.

The objective of BO in this study is to explore the set of variables, w_1, w_2, w_3, t_1, t_2, and Λ, that maximize the FOM_{total} with the smallest computational cost. BO was conducted in the manner shown in Fig. 2. The optimization program was coded using scikit-learn, a library developed for Python[28]. First, the FOMs for 20 random geometries were obtained through preliminary FDTD simulations. The results were accumulated as training data for BO. Second, the program generated a Gaussian process that assumed a numerical model, a relation among FOMs and variables from a database. The Gaussian process also calculated standard deviations of the numerical model to evaluate probability density functions for unanalyzed variables. Third, referring to the

probability density function, the program proposed a new variable candidate to exceed the maximum FOM within the database. It is notable that the program sometimes proposed a candidate value outside of a well-investigated range to avoid falling into a local maximum because the standard deviation tends to be large in this case. Fourth, the absorptivity for the periodic slab with new variables was evaluated through FDTD simulation and its FOM was also evaluated. The FOM for the variables was added to the database to update the Gaussian process model. Then, a new candidate value was proposed. The routine was iterated until the number of calculations, n_c, reached a termination number, N_t. Even if the total number of candidates is larger than several million, a few percent of the candidates is sufficient for N_t to derive optimized parameters [29].

To evaluate the effect of the number of slabs with different widths, BO in the current study was also applied for two reduced geometries, one or two isolated slabs. The range of variables is summarized in Table 2. Here, the width of each slab has a relation, $w_1 < w_2 < w_3$. The increments of all variables were set to 100 nm. In the current optimization, the pitch, Λ, was dependent on the number of slabs, n, slab widths, and thicknesses to maintain the aspect ratio of the gap between two slabs equal to 1.0, as follows:

$$\Lambda = \sum_{k=1}^{n} (w_k + t_1 + t_2). \tag{10}$$

The total number of candidates reached twenty thousand, especially for the triple slab case. However, the computational time of FDTD simulation for each candidate increased

with the number of slabs. Termination was provisionally set to 300 iterations, considering the computational duration. As an exception, all the candidates, including training data for the multilayer with one slab, were calculated since the simulation for a single slab required much less computational time than other conditions.

Table 2 Range of variables in each geometry

Variable	Triple slab	Double slab	Single slab
w_1 (nm)	1600 - 3800	1600 - 3900	1600 - 4000
w_2 (nm)	1700 - 3900	1700 - 4000	—
w_3 (nm)	1800 - 4000	—	—
t_1 (nm)	200 - 500	200 - 500	200 - 500
t_2 (nm)	100 - 300	100 - 300	100 - 300
Total candidates (—)	27600	3600	300
N_t (—)	300	300	280

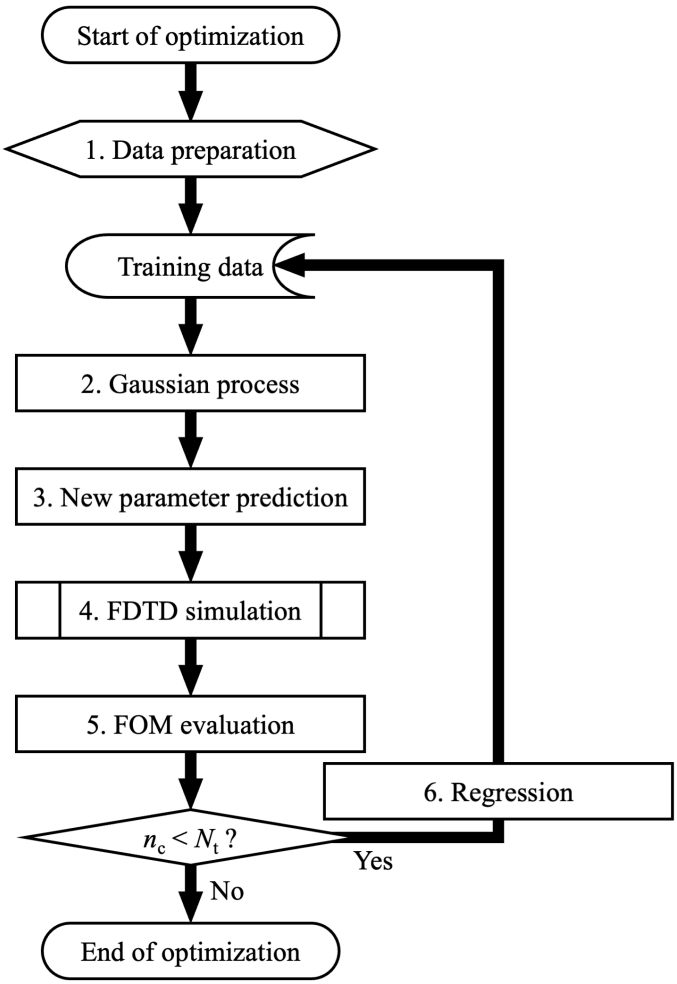

Fig. 2 Optimization flowchart of the current study.

4. Simulation results and discussion

Fig. 3(a) illustrates the difference in the wavelength range between the radiation from a blackbody at room temperature and the solar spectrum. While the wavelengths of solar rays received at the ground are shorter than 2.5 μm, that of thermal emissions from the ground are much longer. Additionally, the zenith transmittance of the atmosphere, depicted in Fig. 3(b), describes radiation within the wavelength range from 7.5 to 14 μm, which is primarily rejected to outer space. The atmosphere also has high transmittance in the range from 3 to 5.5 μm. However, transmittance affects radiative cooling little because of weak blackbody radiation. Fig. 3(b) also shows the absorptivities of multilayered slabs with i-VO_2 obtained by BO based on the wavelength band of the sunlight and thermal emissions from the ground. The obtained parameters are summarized in Table 3. Since multiple reflections and scatterings in and at the edge of the multilayered slabs increase absorptivity, absorptivities at wavelengths from 0.3 to 2.0 μm are on average higher than 0.75, which is useful for increasing the ambient temperature in cold environments. Conversely, radiative cooling is well suppressed due to little absorptivity at wavelengths from 7.5 to 14 μm because the thickness of each layer is much less than the wavelength. Moreover, the surface phonon polariton was not excited in this wavelength range, contrary to the case with a SiO_2 intermediate layer instead of TiO_2 [15]. Fig. 3(c) shows the absorptivities of the same geometry, replacing i-VO_2 with m-VO_2. The absorptivities related to the atmospheric window show several peaks with broad wavelength bands. The number of peaks increases proportionally with the number of slabs. Absorptivity is preferable for radiative cooling because both local maxima of absorptivity reach unity,

especially for a double slab. In the case of a triple slab, radiative cooling becomes weaker than for the double slab due to suppression of the peak at 8.38 μm. Additionally, absorptivity at the peak for a single slab is approximately 0.8 despite its optimized structure. This is because of comparatively greater sunlight absorption. Since the reflectivity of m-VO_2 is insufficient at visible wavelengths, absorptivity at wavelengths from 0.3 to 1.5 μm became greater than 0.5, which is only a little less than the case with i-VO_2. For a single slab, the structure with higher reflectance in the visible range exhibited a higher FOM_{total} than that at a high absorptivity in the atmospheric window range. The lack of reflectivity inhibits the cooling performance of multilayered slabs in summer. Although further improvements in the visible reflectivity are necessary, BO conducted in this study could not provide better candidates.

Table 3 Geometric parameters obtained from Bayesian optimization

Variable	Triple slab	Double slab	Single slab
Λ (nm)	9800	6300	3600
w_1 (nm)	1700	1700	3100
w_2 (nm)	2500	3000	—
w_3 (nm)	3500	—	—
t_1 (nm)	500	500	400
t_2 (nm)	200	300	100

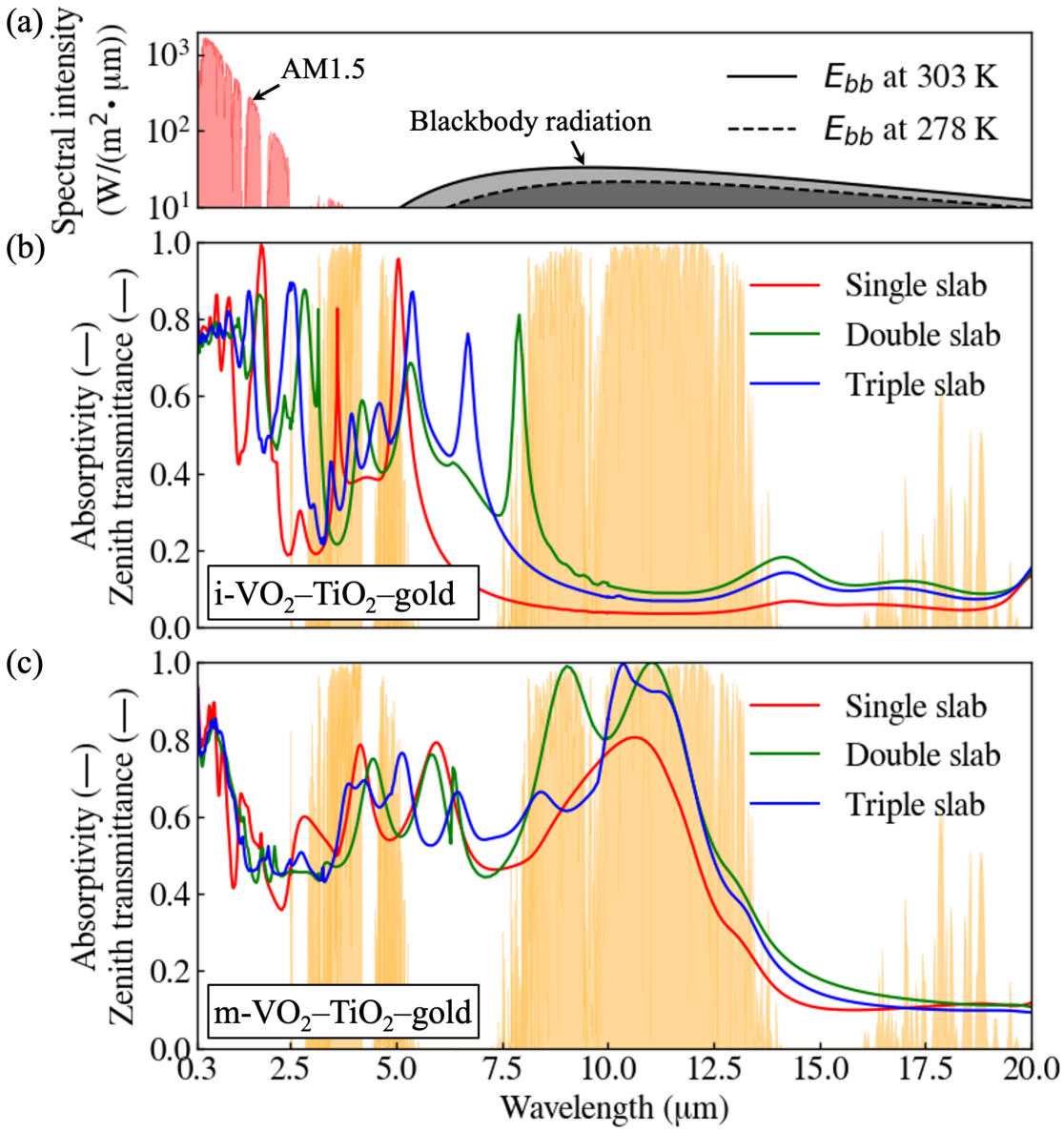

Fig. 3 (a) Spectral intensity of the sunlight and blackbody radiation at 303 and 278 K. Spectral absorptivities of multilayers with (b) insulating and (c) metallic VO_2. The zenith transmittance of the atmosphere is depicted as the simultaneous absorptivities of the multilayers.

Figure 4 shows the progression of maximum FOM developing with the number of calculation iterations. The maximum FOMs continue to saturate until 50 calculation cycles in every case. For the single, double, and triple slab cases, the BO program derived the best candidates after calculating 14.3%, 1.08%, and 0.239% of the total number candidates, including the original training data. Since one calculation cycle in the single, double, and triple slab cases required an average of 0.9, 5.0, and 8.5 hours, BO shows its effectiveness in optimizing nanostructure. This is especially true for the triple slab case with five independent variables and its long computational time. FOM_{hot}, FOM_{cold}, and FOM_{total} for each case are summarized in Table 4. The maximum result for the triple slab case shows a better FOM_{total} than several double slab cases. However, the optimized double slab exhibits the highest FOM_{total}, −39.68, among the three geometries considered in the current study. As shown by the spectral absorptivity in Fig. 3(c), the suppressed absorptivity peak at the wavelength band of the atmospheric window prevents improvements of FOM_{hot}. Here, FOM_{hot} for the theoretical maximum/minimum is derived from Eq. (7), assuming emissivity for sunlight absorption is 0/1.0, while that for radiative cooling is 1.0/0. In the same way, FOM_{cold} for the theoretical maximum/minimum is derived from Eq. (8), assuming emissivity for sunlight absorption is 1.0/0, while that for radiative cooling is 0/1.0. Therefore, FOM_{total} can take values between 556.3 to −694.1. FOMs for three geometries of multilayered slabs are all higher than the theoretical median, −68.9. FOMs for three geometries also exceed the FOM for the gray body, −110.2, which has a constant emissivity of 0.8 for the whole wavelength range. For all cases, the FOM_{cold} of multilayers show positive values. Although FOMs for the multilayered slabs are much

1 better than that for the gray body material, they are still negative due to the low FOM_{hot}
2 originating from high sunlight absorption in summer. However, the whitest paint made of
3 $BaSO_4$ demonstrated by Li *et al*. solves the issue of sunlight absorption and its FOM_{total}
4 becomes a positive value instead of the negative FOM_{cold} [2]. Switching absorptivity
5 related to the radiative cooling was beneficial for improving FOM_{cold}. However, the
6 multilayer could not drastically improve FOM_{hot} due to the reflectivity of m-VO_2,
7 contrary to expectations. Specifically, ω_{l1} for m-VO_2 needs to be much higher to raise
8 reflectivity at visible wavelengths. Since the refractive index of VO_2 is variable and
9 depends on the growth method, improving the fabrication method to obtain higher
10 reflectivity for m-VO_2 film is essential to realizing truly optimized multilayered slabs.
11

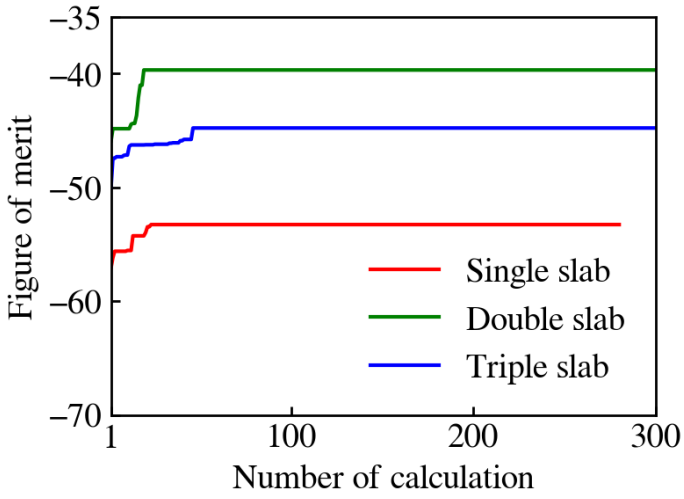

Fig. 4 Improvement process of the maximum value of FOMs.

Table 4 Comparison of FOMs for each geometry and product

Product	FOM_{hot}	FOM_{cold}	FOM_{total}
Single slab	−354.4	301.2	−53.27
Double slab	−336.7	297.0	−39.68
Triple slab	−347.9	303.1	−44.78
Theoretical maximum	142.4	413.9	556.3
Theoretical minimum	−600.1	−93.95	−694.1
Gray body ($\varepsilon = 0.8$)	−366.2	255.9	−110.2
Whitest paint [2]	124.6	−82.07	42.52

To clarify the mechanism of absorptivity enhancement and suppression at high temperatures, electromagnetic energy density distributions around multilayered slabs with the highest FOM_{total} were calculated. Time averaged electromagnetic energy density, $\langle u \rangle$, is obtained from the following equation:

$$\langle u \rangle = \frac{\varepsilon_0}{2}\langle \mathbf{E}^2 \rangle + \frac{\mu_0}{2}\langle \mathbf{H}^2 \rangle, \quad (11)$$

where, ε_0 and μ_0 are the absolute permittivity and magnetic permeability in a vacuum. Figure 5 shows the energy density distributions as responses to monochromatic incident waves corresponding to each absorptivity peak. Each peak is inherent in the resonant modes for every slab. When an incident wave at λ_{r1} = 9.02 μm illuminates a double slab, the electromagnetic energy is concentrated on the side and bottom surfaces of the first m-VO_2 slab. Conversely, only the second slab excites the electromagnetic field for an incident wave at λ_{r2} = 11.03 μm. The interesting point is the decorrelation between the magnitude of energy density and absorptivity. For the same slab, the energy density at the resonant wavelength is higher than at the other wavelength. However, although the magnitude of the relative energy density is much more intense for the first slab at λ_{r1} compared to the second slab at λ_{r2}, both absorptivities are the same and reach values near unity. It is assumed that each slab can excite resonance for an incident wave irradiating a region broader than the slab width, regardless of the electromagnetic energy density.

The resonant wavelength of the electromagnetic field is described as the Fabry–Pérot interference of the short-range surface plasmon polariton (SR-SPP) excited at the surface of m-VO_2 [30,31]. Typical research about SPPs focuses on the longitudinal wave

of an electric charge suspended by a single interface of metal and insulator layers, as shown in Fig. 6(a). Such SPPs can couple to propagating waves using a periodic grating as a coupler. However, when two metal planes facing parallel sandwich an insulating film, as shown in Fig. 6(b), SPPs at the two metal surfaces act to mutually form a coupled mode. The coupled SPP mediated by an anti-symmetrically distributed electric charge is classified as SR-SPP and it is excited by a TM propagating wave [32,33]. The SR-SPPs have a dispersion relation, which is the relation between the angular frequency of incident waves and the wavenumber of SPPs that is different from general SPPs. Here, a complex wavenumber for SR-SPPs, $k_{\mathrm{SPP}}(= k'_{\mathrm{SPP}} + ik''_{\mathrm{SPP}})$ can be defined using k'_{SPP} as a wavenumber and k''_{SPP} as an attenuation coefficient. For $k'_{\mathrm{SPP}} > (\omega/c_0)\sqrt{\varepsilon_{\mathrm{TiO_2\_||}}}$, a TM propagating wave at an angular frequency, ω, can excite the SR-SPPs at a wavenumber, k_{SPP}, satisfying the dispersion relation shown by the following equation:

$$\tanh\left(\gamma_{\mathrm{TiO_2}} t_1\right) + \frac{\varepsilon_{\mathrm{TiO_2\_||}}\gamma_{\mathrm{TiO_2}}\left(\varepsilon_{\mathrm{m-VO_2}}\gamma_{\mathrm{Gold}} + \varepsilon_{\mathrm{Gold}}\gamma_{\mathrm{m-VO_2}}\right)}{\varepsilon_{\mathrm{m-VO_2}}\varepsilon_{\mathrm{Gold}}\gamma^2_{\mathrm{TiO_2}} + \varepsilon^2_{\mathrm{TiO_2\_||}}\gamma_{\mathrm{m-VO_2}}\gamma_{\mathrm{Gold}}} = 0, \tag{12}$$

where, γ_j for each medium is defined using the speed of light in a vacuum, c_0, as follows:

$$\gamma_j^2 = k_{\mathrm{SPP}}^2 - \left(\frac{\omega}{c_0}\right)^2 \varepsilon_j. \tag{13}$$

The red line in Fig. 6(c) shows the dispersion relation of the SR-SPPs for the m-VO_2–TiO_2–gold multilayer. The thickness of TiO_2, t_1, for this calculation is 500 nm. The TM propagating wave with wavelengths shorter than 12 μm excites the SR-SPPs with several times larger wavenumbers than the propagating wave in a vacuum. Moreover, SR-SPPs are reflected at the end of a finite width multilayered slab. Since the reflection of SR-SPPs exhibits Fabry–Pérot-like interference, knowledge of the wavenumber of SR-SPPs and

the slab width is essential to determine the resonant wavelength [30–32,34,35]. For a slab width, w_i, SR-SPPs satisfying the following formula are excited:

$$k'_{\mathrm{SPP}} w_i + \phi_i = m\pi, \tag{14}$$

where, ϕ_i is phase retardation at the terminus of the waveguide for the i^{th} slab, and m is the resonance order (m = 1, 2, 3…). For m = 1, the resonant wavelength can be estimated by comparing k'_{SPP} from Eq. (14) to the dispersion relation of Eq. (12), as shown by the green lines in Fig. 6(c). For the first and second slabs, the peak wavelengths from the simulation, λ_{r1} and λ_{r2}, correspond to the resonant wavelengths with phase retardations of ϕ_1 and ϕ_2 respectively set to 0.20π and 0.16π. This correspondence supports the hypothesis that the oscillation of SR-SPPs induces localization of energy density at the corner of m-VO_2 slabs, as shown in Fig. 5. The blue line in Fig. 6(c) shows the attenuation coefficient of SR-SPPs. At λ_{r1} and λ_{r2}, k''_{SPP} is approximately 2 × 10^5 2π m^{-1}. Thus, the propagation length, $2\pi/k''_{\mathrm{SPP}}$, reaches 30 μm until the SR-SPPs attenuates to e^{-1} times the initial intensity. Since the propagation length is much longer than the slab width of interest, SR-SPPs generated by incident waves are repeatedly reflected at the terminus and absorbed by the slab. A slab with a smaller width requires a larger number of reflections. Therefore, the energy density with a smaller slab width had a larger magnitude compared to wider slabs, and the absolute magnitude does not directly affect the peak absorptivity.

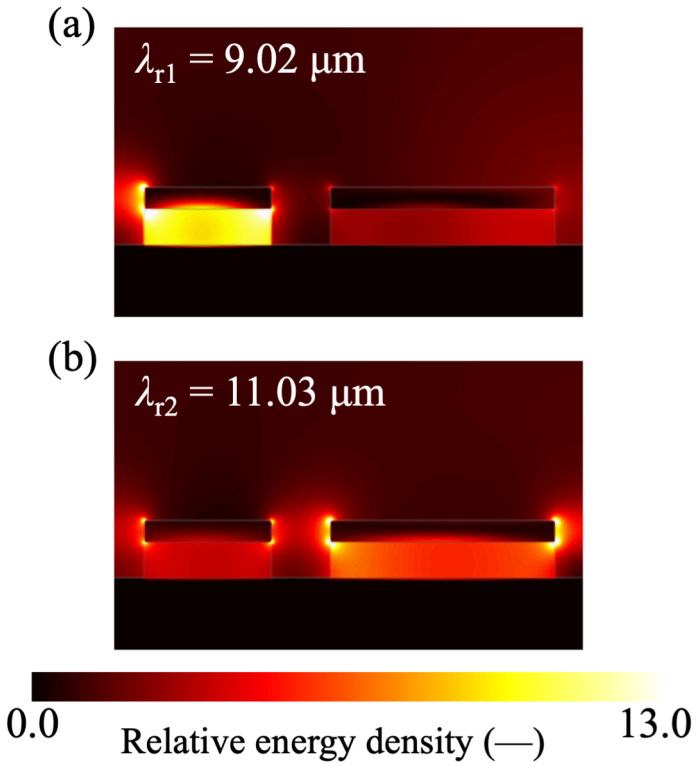

Fig. 5 Contour maps of electromagnetic energy density distribution around double multilayered slabs of different widths. These slabs are illuminated by a monochromatic wave of light at wavelengths of (a) 9.02 and (b) 11.03 μm.

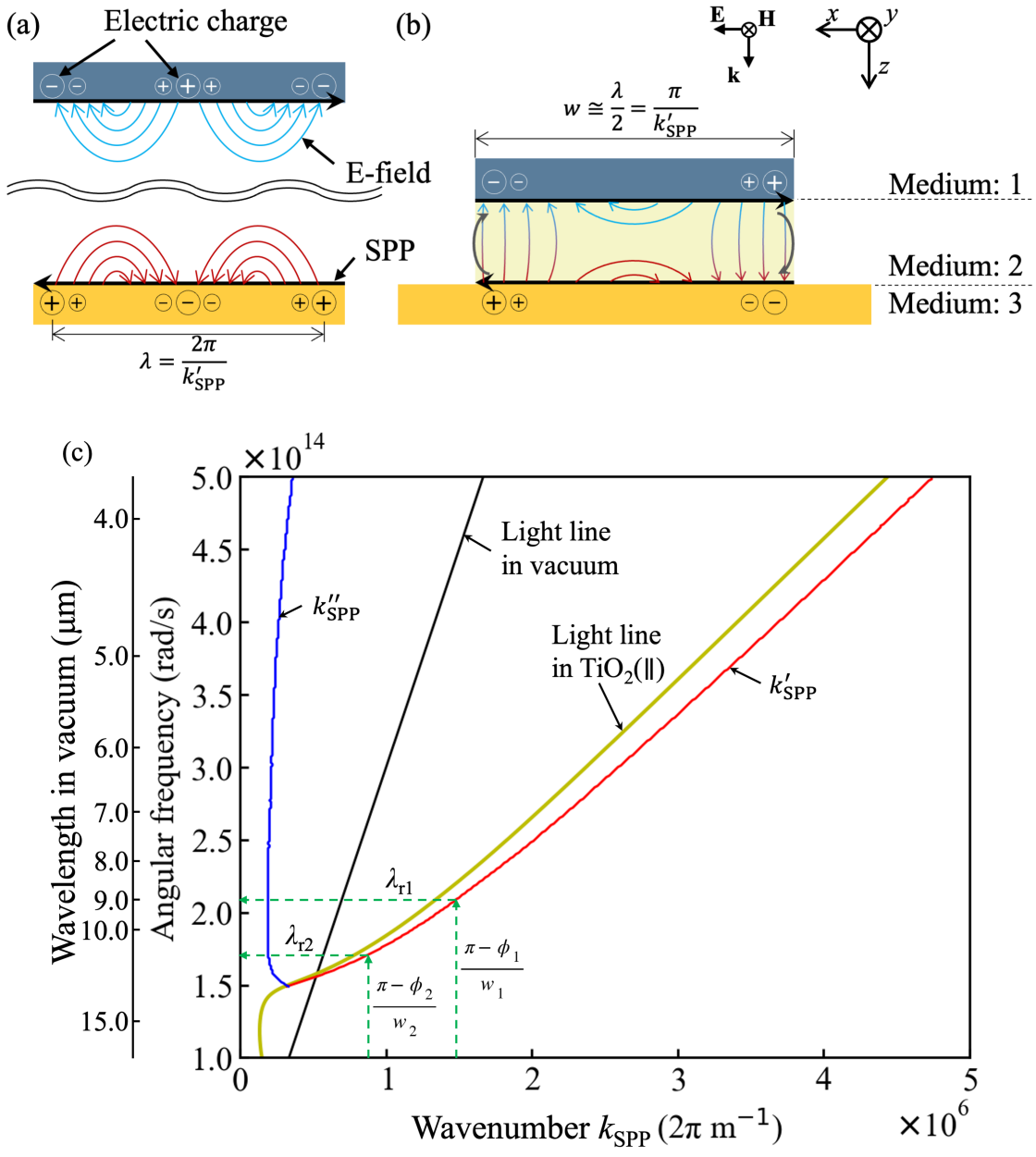

Fig. 6 Schematic diagrams of (a) the SPPs excited along the metal–insulator interface and (b) SPPs' coupled mode maintained between two metal layers sandwiching an insulator. (c) Dispersion relations of the SR-SPP supported by the m-VO_2–TiO_2–gold multilayer. The wavenumber, k'_{SPP}, is depicted by the red line, while the attenuation component, k''_{SPP}, is represented by the blue line.

Figure 7 illustrates the energy density distributions as responses to monochromatic incident waves for the triple slab case. When an incident wave at an 8.38 μm wavelength illuminates a triple slab, the electromagnetic energy is only concentrated around the first slab. While the electromagnetic wave close to the first slab was absorbed by resonance, the wave illuminating the gap between the second and third slabs was reflected by the multilayer. As a result, the absorptivity at the peak was suppressed to a level lower than 0.7. Conversely, the peak absorptivity reached unity at λ = 10.36 μm because the first and third slabs faintly excite the electromagnetic field despite slight deviation from the resonant wavelengths, in addition to excitation of the second slab. All slabs were equally excited to absorb the incident wave for the third peak at λ = 11.18 μm. Thus, peak absorptivity was higher than 0.9. These energy density distributions clarified that the capability of each slab to couple with the incident wave, irradiating a broader region was much more important to improving absorptivity than the intensity of locally confined electromagnetic fields. This finding shows that a moderate energy concentration is sufficient to achieve an absorptivity of 1.0. Furthermore, since each slab can only absorb incident rays passing a narrow cross-section, increasing the number of slabs with different widths is only beneficial in special cases. Among them, the double slab case showed the best result in radiative cooling because both slabs could absorb the entire incident ray.

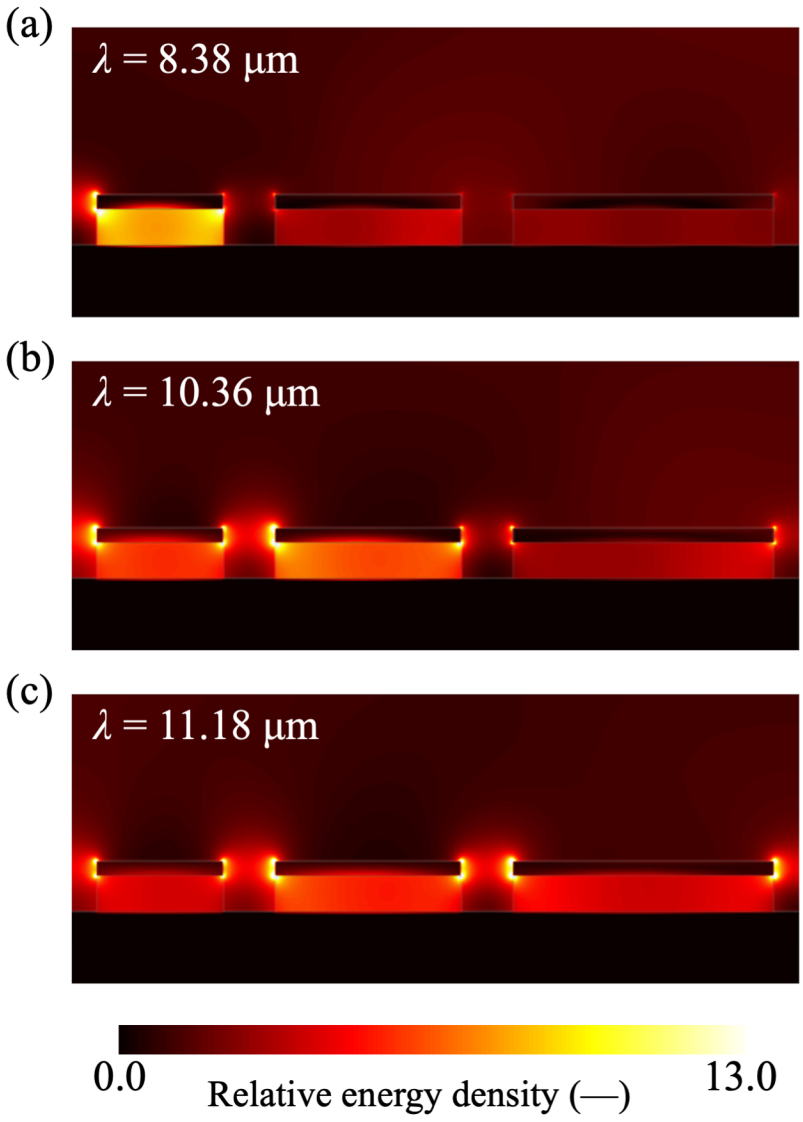

Fig. 7 Contour maps of electromagnetic energy density distribution around three multilayered slabs illuminated by a monochromatic wave. The intensity is normalized according to the intensity of an incident wave. The illumination wavelengths are (a) 8.38, (b) 10.36, and (c) 11.18 μm.

5. Conclusions

In this study, BO investigations for three types of multilayered slabs consisting of VO_2 were conducted to determine the best geometry for passively controlling sunlight absorption and radiative cooling. Optimized geometric parameters were obtained with regression analysis for a few percent of the total number of candidates, particularly the double and triple slab cases. While the optimized structures with i-VO_2 showed low absorptivities in the wavelength range of the atmospheric window, those with m-VO_2 showed broad absorptivity peaks originating from SR-SPPs. Additionally, the structure with i-VO_2 also showed high absorptivities utilizing optical interference in the visible range. The SR-SPPs were locally distributed at the side surface of the m-VO_2 slab and enhanced the electromagnetic energy density as a response to incident waves at the resonant wavelength. For the double slab case, since each slab could couple with an incident wave irradiated upon the whole surface area, peak absorptivity reached 1.0. However, the peak absorptivity of the first slab resonance was suppressed for the triple slab case despite the intensified electromagnetic field confinement. Each slab could interact with an electromagnetic wave irradiated within a limited area. Therefore, the peak absorptivity decreased when the number of slabs was greater than three. Although the double slab showed promising absorptivity at infrared wavelengths, the FOM_{hot} and FOM_{total} still had negative values due to the poor reflectivity of m-VO_2 in the visible range. Further improvements in crystal growth techniques to obtain VO_2 with high visible reflectivity is a remaining issue that needs to be resolved to progress to passive absorptivity control.

Acknowledgement

The authors would like to thank the Japan Society for the Promotion of Science (JSPS) KAKENHI Grant in Aide for Early-Career Scientists (Number: 22K14192) for their financial support.

References

[1] A. Raman, M.A. Anoma, L. Zhu, E. Rephaeli, S. Fan, Passive radiative cooling below ambient air temperature under direct sunlight, Nature. 515 (2014) 540–544. https://doi.org/10.1038/nature13883.

[2] X. Li, J. Peoples, P. Yao, X. Ruan, Ultrawhite $BaSO_4$ paints and films for remarkable daytime subambient radiative cooling, ACS Appl Mater Interfaces. 13 (2021) 21733–21739. https://doi.org/10.1021/acsami.1c02368.

[3] Z. Tong, J. Peoples, X. Li, X. Yang, H. Bao, X. Ruan, Electronic and phononic origins of $BaSO_4$ as an ultra-efficient radiative cooling paint pigment, Materials Today Physics. 24 (2022) 100658. https://doi.org/10.1016/j.mtphys.2022.100658.

[4] T.C. Chang, X. Cao, S.H. Bao, S.D. Ji, H.J. Luo, P. Jin, Review on thermochromic vanadium dioxide based smart coatings: from lab to commercial application, Adv Manuf. 6 (2018) 1–19. https://doi.org/10.1007/s40436-017-0209-2.

[5] A. Ueno, J. Kim, H. Nagano, Thermophysical properties of metal-insulator transition materials during phase transition for thermal control devices, Int J Heat Mass Transf. 166 (2021) 120631. https://doi.org/10.1016/j.ijheatmasstransfer.2020.120631.

[6] M. Kong, K. Egbo, C.P. Liu, M.K. Hossain, C.Y. Tso, C.Y. Hang Chao, K.M. Yu, Rapid thermal annealing assisted facile solution method for tungsten-doped vanadium dioxide thin films on glass substrate, J Alloys Compd. 833 (2020) 155053. https://doi.org/10.1016/j.jallcom.2020.155053.

[7] Y. Jiazhen, Z. Yue, H. Wanxia, T. Mingjin, Effect of Mo-W Co-doping on semiconductor-metal phase transition temperature of vanadium dioxide film, Thin Solid Films. 516 (2008) 8554–8558. https://doi.org/10.1016/j.tsf.2008.05.021.

[8] S. Chen, H. Ma, J. Dai, X. Yi, Nanostructured vanadium dioxide thin films with low phase transition temperature, Appl Phys Lett. 90 (2007). https://doi.org/10.1063/1.2712427.

[9] K. Okimura, J. Sakai, Changes in lattice parameters of VO_2 films grown

on *c*-plane Al_2O_3 substrates across metal–insulator transition, Jpn J Appl Phys. 48 (2009) 045504. https://doi.org/10.1143/JJAP.48.045504.

[10] Y. Muraoka, Y. Ueda, Z. Hiroi, Large modification of the metal–insulator transition temperature in strained VO_2 films grown on TiO_2 substrates, Journal of Physics and Chemistry of Solids. 63 (2002) 965–967. https://doi.org/10.1016/S0022-3697(02)00098-7.

[11] G. Eres, S. Lee, J. Nichols, C. Sohn, J.M. Ok, A.R. Mazza, C. Liu, G. Duscher, H.N. Lee, D.E. McNally, X. Lu, M. Radovic, T. Schmitt, Versatile tunability of the metal insulator transition in $(TiO_2)_m$ /$(VO_2)_m$ superlattices, Adv Funct Mater. 30 (2020) 2004914. https://doi.org/10.1002/adfm.202004914.

[12] K. Ito, T. Watari, K. Nishikawa, H. Yoshimoto, H. Iizuka, Inverting the thermal radiative contrast of vanadium dioxide by metasurfaces based on localized gap-plasmons, APL Photonics. 3 (2018) 086101. https://doi.org/10.1063/1.5025947.

[13] C.-L. Zhou, X.-H. Wu, Y. Zhang, H.-L. Yi, Amplification and modulation effect of elliptical surface polaritons on a thermal diode, Int J Heat Mass Transf. 180 (2021) 121794. https://doi.org/10.1016/j.ijheatmasstransfer.2021.121794.

[14] J.-L. Fang, L. Qu, Y. Zhang, H.-L. Yi, Active control of near-field radiative heat transfer between nanoparticles and slab via the multilayered surface modes, Int J Heat Mass Transf. 200 (2023) 123515. https://doi.org/10.1016/j.ijheatmasstransfer.2022.123515.

[15] K. Isobe, M. Tomioka, Y. Yamada, A. Horibe, Absorptivity control over the visible to mid-infrared range using a multilayered film consisting of thermochromic vanadium dioxide, Int J Thermophys. 43 (2022) 44. https://doi.org/10.1007/s10765-021-02944-4.

[16] Y. Cui, J. Xu, K. Hung Fung, Y. Jin, A. Kumar, S. He, N.X. Fang, A thin film broadband absorber based on multi-sized nanoantennas, Appl Phys Lett. 99 (2011) 253101. https://doi.org/10.1063/1.3672002.

[17] H. Hoshino, K. Okimura, I. Yamaguchi, T. Tsuchiya, Infrared-light switching in highly oriented VO_2 films on ZnO-buffered glasses with controlled phase transition temperatures, Solar Energy Materials and

Solar Cells. 191 (2019) 9–14. https://doi.org/10.1016/j.solmat.2018.10.022.

[18] A. Sakurai, B. Zhao, Z.M. Zhang, Resonant frequency and bandwidth of metamaterial emitters and absorbers predicted by an RLC circuit model, J Quant Spectrosc Radiat Transf. 149 (2014) 33–40. https://doi.org/10.1016/j.jqsrt.2014.07.024.

[19] A.F. Oskooi, D. Roundy, M. Ibanescu, P. Bermel, J.D. Joannopoulos, S.G. Johnson, Meep: A flexible free-software package for electromagnetic simulations by the FDTD method, Comput Phys Commun. 181 (2010) 687–702. https://doi.org/10.1016/j.cpc.2009.11.008.

[20] E.D. Palik., Handbook of Optical Constants of Solids: Volume 1., Academic Press, San Diego, California, 1985.

[21] C. Wan, Z. Zhang, D. Woolf, C.M. Hessel, J. Rensberg, J.M. Hensley, Y. Xiao, A. Shahsafi, J. Salman, S. Richter, Y. Sun, M.M. Qazilbash, R. Schmidt-Grund, C. Ronning, S. Ramanathan, M.A. Kats, On the optical properties of thin-film vanadium dioxide from the visible to the far infrared, Ann Phys. 531 (2019) 1900188. https://doi.org/10.1002/andp.201900188.

[22] T. Kishio, H. Kaneko, K. Funatsu, Strategic parameter search method based on prediction errors and data density for efficient product design, Chemometrics and Intelligent Laboratory Systems. 127 (2013) 70–79. https://doi.org/10.1016/j.chemolab.2013.06.002.

[23] J. Snoek, H. Larochelle, R.P. Adams, Practical Bayesian optimization of machine learning algorithms, Adv Neural Inf Process Syst. 4 (2012) 2951–2959. http://arxiv.org/abs/1206.2944.

[24] E. Contal, V. Perchet, N. Vayatis, Gaussian process optimization with mutual information, 31st International Conference on Machine Learning, ICML 2014. 2 (2013) 1515–1523. http://arxiv.org/abs/1311.4825.

[25] C.A. Gueymard, Parameterized transmittance model for direct beam and circumsolar spectral irradiance, Solar Energy. 71 (2001) 325–346. https://doi.org/10.1016/S0038-092X(01)00054-8.

[26] A. Dudhia, The Reference Forward Model (RFM), J Quant Spectrosc

Radiat Transf. 186 (2017) 243–253. https://doi.org/10.1016/j.jqsrt.2016.06.018.

[27] I.E. Gordon, L.S. Rothman, R.J. Hargreaves, R. Hashemi, E.V. Karlovets, F.M. Skinner, E.K. Conway, C. Hill, R.V. Kochanov, Y. Tan, P. Wcisło, A.A. Finenko, K. Nelson, P.F. Bernath, M. Birk, V. Boudon, A. Campargue, K.V. Chance, A. Coustenis, B.J. Drouin, J. –M. Flaud, R.R. Gamache, J.T. Hodges, D. Jacquemart, E.J. Mlawer, A.V. Nikitin, V.I. Perevalov, M. Rotger, J. Tennyson, G.C. Toon, H. Tran, V.G. Tyuterev, E.M. Adkins, A. Baker, A. Barbe, E. Canè, A.G. Császár, A. Dudaryonok, O. Egorov, A.J. Fleisher, H. Fleurbaey, A. Foltynowicz, T. Furtenbacher, J.J. Harrison, J. –M. Hartmann, V. –M. Horneman, X. Huang, T. Karman, J. Karns, S. Kassi, I. Kleiner, V. Kofman, F. Kwabia–Tchana, N.N. Lavrentieva, T.J. Lee, D.A. Long, A.A. Lukashevskaya, O.M. Lyulin, V.Yu. Makhnev, W. Matt, S.T. Massie, M. Melosso, S.N. Mikhailenko, D. Mondelain, H.S.P. Müller, O.V. Naumenko, A. Perrin, O.L. Polyansky, E. Raddaoui, P.L. Raston, Z.D. Reed, M. Rey, C. Richard, R. Tóbiás, I. Sadiek, D.W. Schwenke, E. Starikova, K. Sung, F. Tamassia, S.A. Tashkun, J. Vander Auwera, I.A. Vasilenko, A.A. Vigasin, G.L. Villanueva, B. Vispoel, G. Wagner, A. Yachmenev, S.N. Yurchenko, The HITRAN2020 molecular spectroscopic database, J Quant Spectrosc Radiat Transf. 277 (2022) 107949. https://doi.org/10.1016/j.jqsrt.2021.107949.

[28] F. Pedregosa, G. Varoquaux, A. Gramfort, V. Michel, B. Thirion, O. Grisel, M. Blondel, P. Prettenhofer, R. Weiss, V. Dubourg, J. Vanderplas, A. Passos, D. Cournapeau, M. Brucher, M. Perrot, E. Duchesnay, Scikit-learn: Machine Learning in Python, Journal of Machine Learning Research. 12 (2011) 2825–2830. http://jmlr.org/papers/v12/pedregosa11a.html.

[29] A. Sakurai, K. Yada, T. Simomura, S. Ju, M. Kashiwagi, H. Okada, T. Nagao, K. Tsuda, J. Shiomi, Ultranarrow-band wavelength-selective thermal emission with aperiodic multilayered metamaterials designed by Bayesian optimization, ACS Cent Sci. 5 (2019) 319–326. https://doi.org/10.1021/acscentsci.8b00802.

[30] T. Liu, J. Takahara, Ultrabroadband absorber based on single-sized embedded metal-dielectric-metal structures and application of radiative cooling, Opt Express. 25 (2017) A612. https://doi.org/10.1364/OE.25.00A612.
[31] K. Isobe, K. Hanamura, Resonance modes of a metal-semiconductor-metal multilayer mediated by electric charge, J Phys Commun. 6 (2022) 045006. https://doi.org/10.1088/2399-6528/ac678f.
[32] S.I. Bozhevolnyi, T. Søndergaard, General properties of slow-plasmon resonant nanostructures: nano-antennas and resonators, Opt Express. 15 (2007) 10869. https://doi.org/10.1364/OE.15.010869.
[33] W. Bai, Q. Gan, G. Song, L. Chen, Z. Kafafi, F. Bartoli, Broadband short-range surface plasmon structures for absorption enhancement in organic photovoltaics, Opt Express. 18 (2010) A620. https://doi.org/10.1364/OE.18.00A620.
[34] S.I. Bozhevolnyi, Plasmonic Nanoguides and Circuits, Pan Stanford Publishing Pte., 2009.
[35] E.S. Barnard, J.S. White, A. Chandran, M.L. Brongersma, Spectral properties of plasmonic resonator antennas, Opt Express. 16 (2008) 16529. https://doi.org/10.1364/OE.16.016529.